

Monitoring changes in velocity and Q using non-physical arrivals in seismic interferometry

Deyan Draganov, Ranajit Ghose, Karel Heller and Elmer Ruigrok

Department of Geoscience & Engineering Delft University of Technology, Stevinweg 1, 2628 CN, Delft, The Netherlands. E-mail: d.s.draganov@tudelft.nl

Accepted 2012 October 18. Received 2012 October 12; in original form 2011 December 20

SUMMARY

Application of seismic interferometry to records from receivers at the Earth's surface from sources in wells retrieves the reflection response measured at the receivers as if from virtual sources located also at the surface. When the wavefields experience intrinsic losses during propagation, non-physical arrivals (ghosts) would appear in the retrieved result. These ghosts appear due to waves that reflect inside a subsurface layer. Thus, a ghost contains information about the seismic properties of the specific layer. We show how such ghosts can be used to monitor layer-specific changes in the velocity and intrinsic losses in the subsurface. We show how to identify the ghosts using numerical-modelling results from a vertical well, and how to estimate the layer-specific velocity and quality-factor changes using numerical-modelling results from a horizontal well as well as ultrasonic S -wave laboratory data.

Key words: Downhole methods; Interferometry; Controlled source seismology; Body waves; Seismic attenuation.

1 INTRODUCTION

It has been shown that by cross-correlating seismic traces recorded at two receivers, the Green's function between these two receivers can be retrieved as if one of the receivers were a virtual seismic source (e.g. Schuster 2001; Wapenaar *et al.* 2002; Campillo & Paul 2003; Schuster *et al.* 2004; Snieder 2004; Wapenaar 2004). In this framework, transient or (white) noise sources can be used and they should completely surround the two receivers (Wapenaar & Fokkema 2006). This retrieval process is commonly termed seismic interferometry (SI). When the retrieval is performed with receivers at the Earth's surface (which we consider hereinafter), only sources in the subsurface are required. This is due to the fact that the Earth's surface is a free surface for seismic waves and acts as a mirror creating reflection of the subsurface sources, thus effectively making a closed boundary. The exact acoustic SI relation requires two types of sources—monopole and dipole—to be present at the same positions along the source boundary in the subsurface. For practical applications in the field, this is not a likely situation. Therefore, high-frequency and far-field approximations are made to reach a more practical relation, where the approximations result in mainly amplitude errors (Wapenaar & Fokkema 2006). For an acoustic medium, this relation is (Wapenaar & Fokkema 2006)

$$G(\mathbf{x}_B, \mathbf{x}_A, t) + G(\mathbf{x}_A, \mathbf{x}_B, -t) \approx \frac{2}{\rho c} \oint_{\partial\mathbb{D}} G(\mathbf{x}_B, \mathbf{x}, t) * G(\mathbf{x}_A, \mathbf{x}, -t) d^2\mathbf{x}, \quad (1)$$

where c and ρ are the constant propagation velocity and mass density at and outside of the source-boundary surface $\partial\mathbb{D}$, which is assumed

to encompass the medium of interest with the two receivers positioned at \mathbf{x}_A and \mathbf{x}_B at the Earth's surface, and $*$ denotes convolution. $G(\mathbf{x}_B, \mathbf{x}_A, t)$ is the Green's function between a source at \mathbf{x}_A and a receiver at \mathbf{x}_B , while $G(\mathbf{x}_B, \mathbf{x}_A, -t)$ is its time-reversed variant. The right-hand side of relation (1) is the cross-correlation of recordings at the points \mathbf{x}_A and \mathbf{x}_B from sources at positions \mathbf{x} on $\partial\mathbb{D}$ in the subsurface. Note that this relationship assumes that the medium at and outside $\partial\mathbb{D}$ is homogeneous. When this is not the case, non-physical arrivals appear in the retrieved results. Such arrivals can become weaker or even disappear if $\partial\mathbb{D}$ is sufficiently irregular, where the irregularity is model- and scale-dependent (Draganov *et al.* 2004). We shall recall this issue in Section 4.

Relation (1) is valid when the boundary sources emit the same energy, have regular spacing and are spaced densely enough. When these requirements are not met, non-physical arrivals (ghosts) may appear in the retrieved Green's function due to insufficient destructive interference in the summation process in relation (1) of events caused by scattering between inhomogeneities inside the medium (Snieder *et al.* 2006; Mehta *et al.* 2008; Vasconcelos *et al.* 2009). Furthermore, due to insufficient constructive interference, the physical arrivals might be retrieved with incorrect phase (e.g. Froment *et al.* 2010). Note that the ghost arrivals can be very useful. One example of useful ghosts is the virtual refraction (Dong *et al.* 2006; Tatanova *et al.* 2008; Mikesell *et al.* 2009; Bharadwaj *et al.* 2011). These ghosts are easily identified because they pass through the virtual-source position at $t = 0$ s and have a linear moveout. They can be used to estimate the propagation velocity of P - or S -waves of subsurface layers, for example where the standard refraction method cannot be used (Nichols *et al.* 2011; Tatanova *et al.* 2011). Other useful ghosts are the spurious (peg-leg) multiples as described by

Snieder *et al.* (2006), which represent reflection energy. King *et al.* (2011) showed that these ghosts can be used in velocity analysis to obtain an estimate of the subsurface velocities. For the marine case of towed streamers of sources and receivers, King & Curtis (2012) showed that the spurious multiples can be identified when the results retrieved by SI by cross-correlation are compared with results from source-receiver interferometry (Curtis & Halliday 2010). Furthermore, King *et al.* (2011) used this type of ghost to estimate interval velocities for each layer in the subsurface.

Relation (1) is derived for the case of a lossless medium. When the wavefields experience intrinsic losses inside $\partial\mathbb{D}$, eq. (1) should be modified to include cross-correlations from sources inside the complete volume \mathbb{D} enclosed by the boundary $\partial\mathbb{D}$ (Snieder 2006; Wapenaar *et al.* 2006; Snieder 2007; Vasconcelos *et al.* 2009)

$$\begin{aligned} & G(\mathbf{x}_B, \mathbf{x}_A, t) + G(\mathbf{x}_A, \mathbf{x}_B, -t) \\ & \approx \frac{2}{\rho c} \oint_{\partial\mathbb{D}} G(\mathbf{x}_B, \mathbf{x}, t) * G(\mathbf{x}_A, \mathbf{x}, -t) d^2\mathbf{x} \\ & + \int_{\mathbb{D}} [b^p(\mathbf{x}, t) + b^p(\mathbf{x}, -t)] * G(\mathbf{x}_B, \mathbf{x}, t) * G(\mathbf{x}_A, \mathbf{x}, -t) d^3\mathbf{x}, \end{aligned} \quad (2)$$

where it is assumed that the volumetric source distribution is proportional to the intrinsic losses. Relation 2 is derived starting from the equation of motion and the stress–strain relation for media with intrinsic losses. The losses are represented by the space-dependent causal loss function $b^p(\mathbf{x})$, which is related to the compressibility (see notation in Wapenaar *et al.* (2006)). The causal loss function related to the mass density is assumed to be zero, but this can be easily accounted for. To further ensure causality, the density and compressibility are taken to be real-valued. In field or laboratory measurements, where intrinsic losses will most likely be present, it will be very difficult to find a situation where the source distribution is volumetric. It is shown that to account for the intrinsic losses, one could use SI by convolution (Slob *et al.* 2007; Halliday & Curtis 2009), trace deconvolution (Vasconcelos & Snieder 2008a,b) or multidimensional deconvolution (Wapenaar *et al.* 2008). Each of these methods has its own additional requirements, which might not always be met. Because of this, in many practical situations one would still resort to relation (1). In such situations, Draganov (2007), Halliday & Curtis (2009), Vasconcelos *et al.* (2009) and Draganov *et al.* (2010) showed that the spurious multiples (hereinafter called reflection ghosts) will appear in the retrieved results even in the case when the boundary sources surround completely the two receivers. In lossless media, the reflection-ghost terms, which contribute to the final retrieved ghost arrivals, mutually cancel each other. Vasconcelos *et al.* (2009) show this with an analytical example for a 1-D medium. They also show that when using scattering-based SI, the same statement is valid when losses are present, but confined only to the localized scattering region. In generally attenuative media, these terms will not mutually cancel, as one of them will be weaker due to the experienced intrinsic losses (e.g. Draganov *et al.* 2010). When only identification and possible removal of the ghosts is of interest, Ruigrok *et al.* (2009) showed that the identification can be achieved by correlating the complete trace at one of the receivers with only the first arrival at the other receiver. This results in the ghosts appearing to have stronger amplitudes. On the other hand, Draganov *et al.* (2010) show that ghosts due to intrinsic losses can be used to estimate the quality factor (Q) of the layer causing the reflection ghosts. For this, the authors apply a Q -compensation procedure that requires sources at depth with sufficient illumination

aperture. They show that the ghosts can be identified by the change in the ghosts' polarity, but leave open the question how a specific ghost can be related to a layer that caused it to appear. When the source boundary does not completely enclose the receivers, some of the reflection-ghost terms might not be retrieved. As a result, some portions of a ghost might keep their polarity and thus not be identified as being parts of a retrieved ghost.

For monitoring purposes, quite often the seismic surveys make use of sources at the surface and receivers in wells. For these reasons, we will apply SI to such geometries. Wapenaar & Fokkema (2006) derive representation (1) after application of source-receiver reciprocity to their equation 19. Without application of source-receiver reciprocity, representation (1) can be rewritten as

$$\begin{aligned} & G(\mathbf{x}_B, \mathbf{x}_A, t) + G(\mathbf{x}_A, \mathbf{x}_B, -t) \\ & \approx \frac{2}{\rho c} \oint_{\partial\mathbb{D}} G(\mathbf{x}, \mathbf{x}_B, t) * G(\mathbf{x}, \mathbf{x}_A, -t) d^2\mathbf{x}. \end{aligned} \quad (3)$$

This relation states that we can retrieve the Green's function between two sources from recordings along a boundary of receivers. In the following chapter, we apply eq. (3) to synthetic seismic data in a vertical-well geometry to show how ghosts due to intrinsic losses can be identified and connected to specific layers with attenuation. Furthermore, we apply the relation to synthetic and ultrasonic laboratory examples from a horizontal-well geometry to demonstrate how to use these ghost arrivals to estimate layer-specific changes in velocity and Q using surface sources. Because in practice the surface-source aperture might also be very limited, we make use of a very limited number of surface sources. In fact, we take the extreme case of one source.

2 MONITORING VELOCITY AND Q CHANGES: NUMERICAL EXPERIMENTS

To be able to make use of the ghost due to intrinsic losses, this ghost should first be unambiguously identified and connected to a specific layer that causes it to appear. To achieve the identification, we propose to make use of a vertical-well geometry with a source at the surface.

2.1 Identifying ghost arrivals using a vertical well

We simulate a transmission experiment using a 2-D acoustic finite-difference modelling scheme (Thorbecke & Draganov 2011). Fig. 1 shows the model to simulate recordings from an impulsive source at the surface to receivers along a vertical well. A dipole source at the surface is located at 4000 m horizontal distance. The receivers in the well are between depth levels of 100 and 1090 m at a 15-m interval and they record the vertical component of the particle velocity. The source at the surface is excited and the responses are recorded for 4 s, see Fig. 2(a).

We perform SI by taking the autocorrelation of each trace (Fig. 2 b). Due to the geometry of the vertical well and the source, we do not need multiple receivers, and therefore, we do not need the summation as prescribed by relation (3). If the surface source were a plane wave and the subsurface were 1-D, the result would represent the retrieved 1-D response as if there were a coinciding source and receiver at the surface (Claerbout 1968). In our case, we use a source with finite dimensions that produces waves with geometrical spreading, but we still retrieve the correct arrival times of the reflections from the subsurface layers. The cartoon in Fig. 2(d)

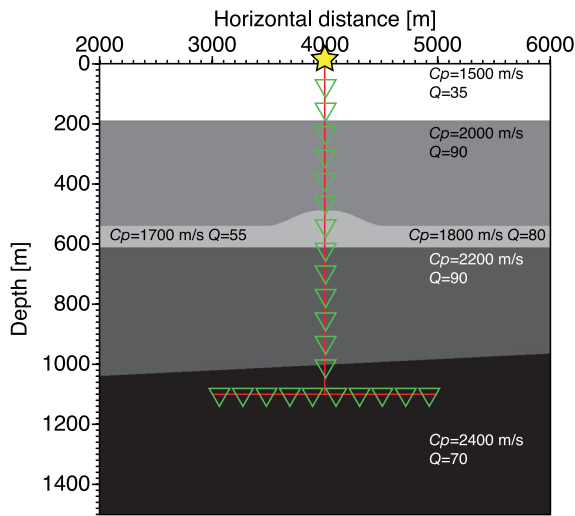


Figure 1. Subsurface model with receivers (green triangles) installed along a vertical and a horizontal well (red lines). The vertical well is instrumented between depths of 100 and 1090 m every 15 m, the horizontal well is instrumented between 3000 and 5000 m horizontal distance every 20 m. The propagation velocity in the layers is denoted by C_p , while Q stands for quality factor.

illustrates retrieval of some events from Fig. 2(b). The retrieved horizontal arrival around 0.25 s is the reflection from the bottom of the first layer and results from the correlation of, for example, the dark blue (direct) and the orange (free-surface multiple) arrivals. The retrieved horizontal arrival at 0.51 s is the multiple of the previous reflection, the horizontal arrival at 0.55 s is the reflection from the bottom of the second layer, while the retrieved horizontal arrival at 0.69 s is the reflection from the bottom of the third layer. Comparing the retrieved result in Fig. 2(b) with the directly modelled reflection response in Fig. 2(c), we can see that apart from these arrivals, there are also ghost events that should not be present in a subsurface

reflection response. (Further in this subsection we show how the ghosts can be identified as such without knowing the subsurface model.) Such are, for example, the three horizontal events retrieved at 0.13, 0.30 and 0.35 s in Fig. 2(b). These three events represent ghosts from reflection inside layers—the earliest ghost is caused by the third layer, the following ghost by the second layer, while the latest ghost by the fourth layer. The origin of these reflection ghosts can be understood using the cartoon in Fig. 2(d). For example, the ghost at 0.30 s arises from the correlation of the dark blue (direct) and the light blue (internal reflection inside the second layer) arrivals in Fig. 2(d). Also correlations of other pairs of arrivals will contribute constructively or destructively to the retrieval of this ghost. Such are the pairs, for which the second arrival has traversed the path of the first one but also includes one extra internal reflection inside the second layer. The finally obtained retrieved ghost can be seen as a reflection from the bottom of the second layer recorded directly at the top of the second layer with coinciding source and receiver. The retrieval of the ghost events at 0.13 and 0.35 s can be explained in a similar way. This means that the two-way traveltime of each of these ghosts corresponds to a specific layer velocity and thickness (Ruigrok *et al.* 2008). The reflection ghost at 0.43 s arises from correlation of arrivals containing internal reflection that has traversed the second and the third layers, so its two-way traveltime is characterized by the effective velocity of these two layers.

In Fig. 2(b), we can also see retrieved inclined arrivals. As we are retrieving the reflection response for coinciding source and receiver at the surface, these are also ghost arrivals (compare with the directly modelled reflection response in Fig. 2(c)). For example, the inclined arrival starting at 0.42 s at depth 100 m and ending at 0 s at 490 m arises from the correlation of the dark blue (direct) with the purple (multiple reflection from the bottom of the second layer) arrival in Fig. 2(d). Because of that, this arrival kinematically represents a reflection as if recorded with coinciding source and receiver at the position of the receiver inside the well. Note that the retrieval of the inclined ghosts arises from correlation of arrivals coming to the receivers from opposite directions (up- and downgoing fields),

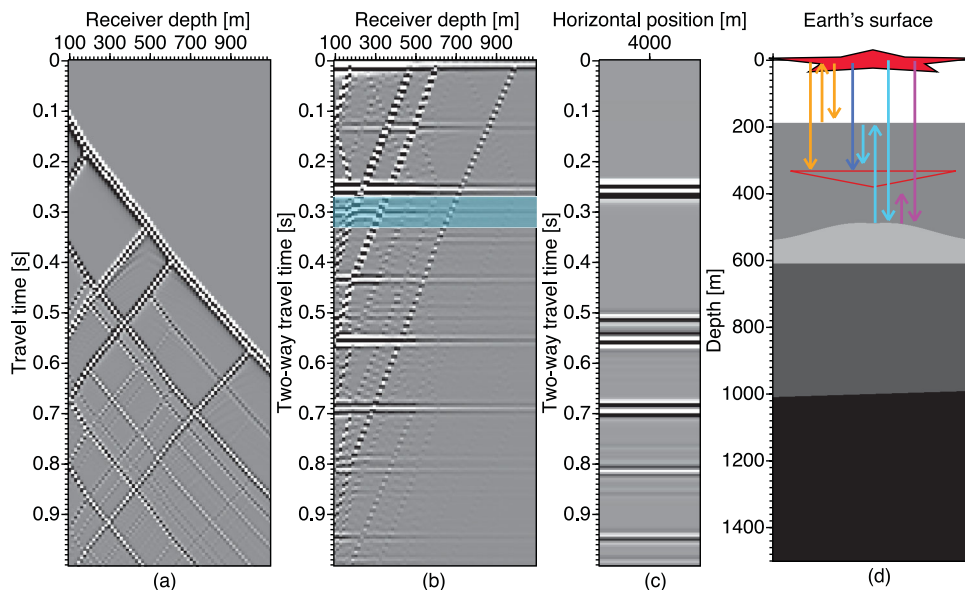


Figure 2. (a) Synthetic transmission wavefield from a source at the surface recorded by receivers in the vertical well. (b) The result of applying seismic interferometry by autocorrelation of each trace in (a). One retrieved ghost arrival is highlighted in transparent blue. (c) Directly modelled reflection response for the same subsurface model. (d) Propagation paths (coloured arrows) of several arrivals. The correlations of different combinations of these arrivals results in the retrieval of physical and non-physical events. The surface source (red star) and the subsurface receiver (triangle) are stretched to illustrate that all the arrivals originate and are recorded by one source and one receiver, respectively.

while the retrieval of the horizontal ghosts arises from correlation of arrivals coming to the receivers from the same direction. If we apply relation (1) and remove the free-surface multiples from the modelled responses (Wapenaar 2006), then the autocorrelation will retrieve recordings as if from coinciding virtual sources and receivers inside the well, making the retrieval process an interferometric redatuming. Consequently, the retrieved inclined arrivals would represent real retrieved reflections from the subsurface layers. The interferometric redatuming could also be achieved by applying correlation after wavefield separation (Bakulin & Calvert 2004, 2006; Vasconcelos *et al.* 2009).

By visually comparing the ghost arrivals with the physical retrieved reflections and their multiples, we see that the ghosts display a polarity reversal once the downhole receiver positions cross the top of the layer causing the ghosts. The physical reflections have a constant polarity. This difference enables us to identify ghost arrivals without knowing the subsurface model and determine which subsurface layer gives rise to a specific ghost. Note that we can use the inclined events to find the bottom of the layers giving rise to the ghosts. Thus, inclined events and polarity change of ghosts give together the thickness of the layers causing the ghosts. For this, though, we have to make a quasi-1-D assumption of the medium. Once we identify the ghosts and connect them to specific layers, we can apply the Q -compensation procedure proposed by Draganov *et al.* (2010) to monitor changes in Q , but also in velocity, inside these layers.

2.2 Monitoring velocity and Q changes using a horizontal well

To develop a method for monitoring velocity and Q changes in layers using identified ghosts, we make use of receivers inside a horizontal well, see again Fig. 1. The horizontal well is instrumented between 3000 and 5000 m, with vertical-particle velocity receivers placed every 20 m. The source at the surface is excited and the responses are recorded along the well for 4 s. Fig. 3(a) shows the modelled

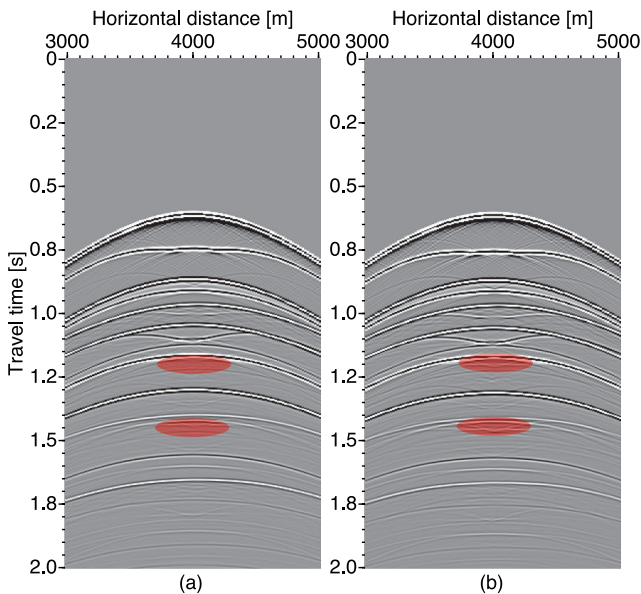


Figure 3. The synthetic transmission response recorded using a source at the surface and receivers in the horizontal well: (a) base survey with velocity $C_p = 1800$ s and quality factor $Q = 80$ in the third layer; (b) monitor survey with velocity $C_p = 1700$ s and quality factor $Q = 55$ in the third layer. The red transparent ellipses indicate changes in the recorded arrivals.

transmission response. For the base survey, the model is given in Fig. 1 with P -wave velocity (C_p) and Q in the third (reservoir) layer equal to 1800 m s^{-1} and 80 , respectively. The geometry we use gives us many subsurface receivers along which we have to integrate, as required by Draganov *et al.* (2010). We apply relation (3) by autocorrelating all traces (the integrand) in the transmission panel and then summing them together (the integration). As we do not have a closed subsurface-receiver boundary, we taper the autocorrelations to zero for receivers at both ends of the horizontal well. The obtained retrieved zero-offset reflection trace for a source and receiver at the surface is shown in Fig. 4(a). The SI result contains retrieved arrivals at both positive and negative times, but as the autocorrelation is symmetric, we use only the positive times.

Along with the physical reflections at 0.25 , 0.51 , 0.55 and 0.69 s in Fig. 4(a), we also see arrivals at 0.13 , 0.3 and 0.35 s. Using the results of applying SI to the data from the vertical well, we can unambiguously interpret these events as ghosts from the third, second and fourth layers, respectively. As each ghost represents a reflection arrival that has propagated only inside one of these three layers, the two-way traveltime of each ghost is a direct indication of the layer's velocity. Knowing the thickness of the layers (from the recordings in the vertical well) we can estimate the layer velocities. After this, we can proceed to estimate the layer-specific Q s.

To estimate the effective Q of the overburden above a ghost-producing layer, we apply the Q -compensation procedure of Draganov *et al.* (2010). The finite-difference modelling scheme that we use applies intrinsic losses to the modelled wavefield as an amplitude damping $e^{-\frac{t\pi f_0}{Q_{\text{layer}}}}$ (Aki & Richards 2002), where f_0 is the centre frequency of the source wavelet and Q_{layer} is the quality factor per layer. Therefore, we apply a gain of $e^{\frac{t\pi f_0}{Q_{\text{trial}}}}$ to the panel in Fig. 4(a). For a Q_{trial} equal to the effective Q of the overburden above a specific ghost-producing layer, the ghost arrival should disappear. When the correct value of Q_{trial} is passed, the ghost should reappear, but with reversed polarity (Draganov *et al.* 2010). Figs 4(b)–(f) show the SI results after applying Q -compensation with various Q_{trial} . We see that the ghost at 0.35 s disappears at $Q_{\text{trial}} = 56.1$ and the ghost at 0.13 s disappears at $Q_{\text{trial}} = 52.3$. This means that these are the values of the effective Q of the overburden down to the fourth and the third (reservoir) layers, respectively. The ghost at 0.3 s does not disappear, as was expected, at $Q_{\text{trial}} = 35$. This happens because a multiple of the ghost at 0.13 s is overlaying the ghost at 0.3 s and they interfere. This impedes the estimation of the effective Q above the second layer (which is in fact the Q of the first layer).

Knowing the effective Q for each layer from the three ghosts would permit us to calculate the intrinsic Q in each layer using

$$Q_{\text{eff}} = \frac{\sum_i \frac{d^i}{C_p^i}}{\sum_i \frac{d^i}{C_p^i Q^i}}, \quad (4)$$

where d^i , C_p^i and Q^i are the thickness, propagation velocity and intrinsic Q for each layer i down to a specific ghost-producing layer. From the ghosts in the SI result, we can calculate the velocity of each layer. As we assume that the thickness of each layer is independently known, we can then calculate the layer-specific intrinsic Q starting from the first layer using eq. (4). In practical situations, the layer thickness might be taken from well data or even from seismic-imaging results. In the former case, the well data should be tied to the seismic data to obtain the same scales; in the later case, the errors in the estimated thickness from imaging will result in errors in the estimated layer-specific intrinsic Q . Any errors in the velocity of the overlying layers will be propagated down to the

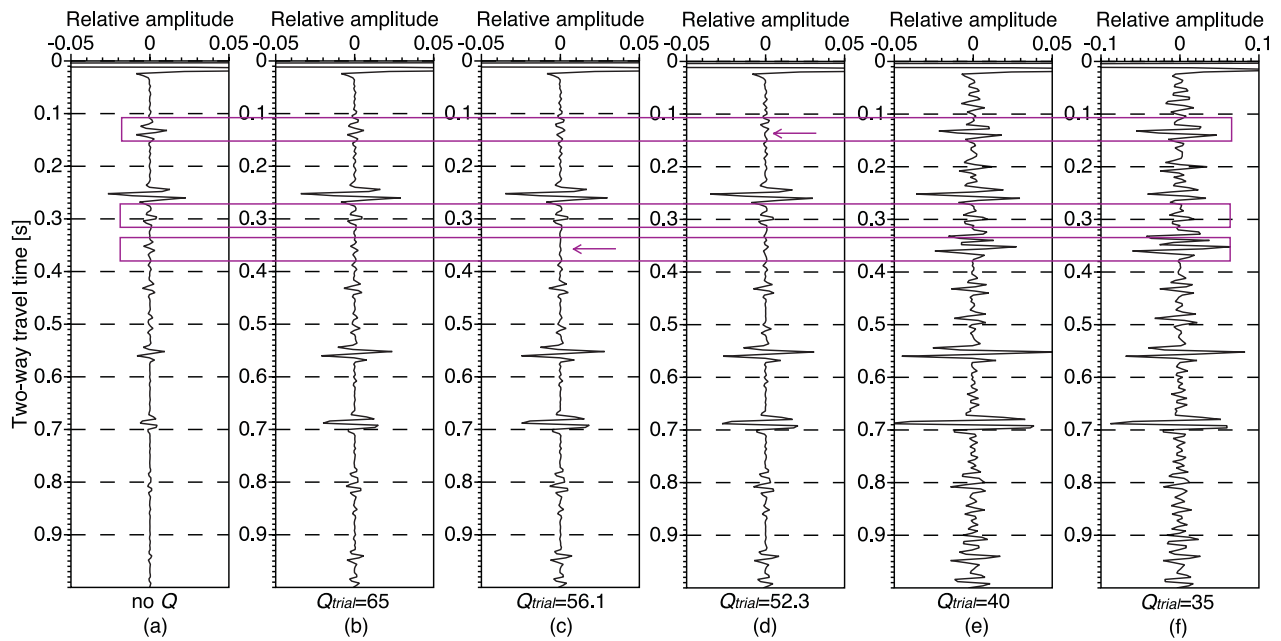


Figure 4. Results from seismic interferometry with and without Q compensation. Each trace represents a retrieved zero-offset trace for a virtual source and receiver at the surface. The purple rectangles indicate the ghost arrivals from the third, second and fourth layers. (a) Retrieved result without Q compensation. (b)–(f) Retrieved results with Q -compensation for Q_{trial} equal to 60, 56.1, 52.3, 40 and 35, respectively. The purple arrows mark the disappearance of a ghost. All amplitudes are normalized to the respective maxima (of the peak at $t = 0$ s).

specific layer of interest and will result in errors. Due to the layer-stripping approach implied in eq. (4), the errors will propagate also in the estimated Q values. In our case, the Q of the first layer cannot be estimated using the above-mentioned procedure; therefore, to use eq. (4), we will have to know the Q of the top layer by some other means, for example, by using the spectral-ratio (SR) method to the measurements in the vertical well (Tonn 1991). Application of the SR method to well data for estimation of Q might also suffer from multiply reflected arrivals coming from the layers below or above the one for which we want to estimate Q (Mateeva 2003). On the other hand, the SI Q -estimation procedure results in calculating the effective losses. Knowing these values down to the second and the third layers, we can calculate directly the losses due to the propagation of the wavefield inside the third layer and from there the intrinsic loss for the third layer. Thus, using the SI Q -estimation procedure, we can obtain the Q -value of the third layer without the application of eq. (4).

Fig. 3(b) shows the modelled response as recorded inside the horizontal well from the source at the surface for a monitor survey. For this monitor survey, the velocity and Q in the reservoir layer are changed to 1700 m s^{-1} and 55, respectively, while the parameters of the other layers remain unchanged. As indicated by the red ellipses in Fig. 3, the changed velocity inside the reservoir results in differences in the recorded arrivals. Fig. 5 shows the results from the Q -compensation procedure for this case. We see that the ghost in the base survey at 0.13 s now arrives at 0.14 s (the identification of the ghost at this new time is performed again using the vertical well). We can use this information to estimate velocity change in the reservoir layer. As explained above, because this ghost represents energy that has propagated inside the reservoir layer, it is only sensitive to changes in this layer. We also see that the ghost from the fourth layer at time 0.35 s does not disappear in Fig. 5(c) at $Q_{\text{trial}} = 56.1$, but instead at $Q_{\text{trial}} = 52.9$ (Fig. 5d). The correct Q_{trial} value of the ghost at 0.13 s did not change, which is expected as the intrinsic losses above this layer did not change between the base and the monitor surveys.

As in the base survey, the ghost at 0.3 s does not disappear due to the interference of the multiple of the earliest ghost. Therefore, we do not show this result. Again, using eq. (3), the change in Q within the reservoir layer can be estimated. In this example, we use constant- Q (i.e. frequency independent) assumption in each layer. However, if this approach of estimation of layer-specific changes in velocity and Q is extended to obtain changes in velocity dispersion and Q -dispersion for poroelastic media, then one could estimate the flow properties (porosity and permeability) in the porous subsurface (Zhubayev & Ghose 2010, 2011, 2012a,b).

3 LABORATORY-DATA EXAMPLE

Next, we demonstrate estimation of velocity and Q changes with an ultrasonic laboratory experiment. We use a two-layer sample with a bottom-layer thickness of 50.7 mm and a top-layer thickness of 30 mm (see Fig. 6 a). For the bottom layer we use aluminium, because the waves experience no detectable attenuation during propagation. For the top layer, we use a plate of Felser sandstone for the base survey and of Portland cement for a monitor survey. The goal is to detect and estimate the changes due to the different top-layer materials. As sources and receivers we use ultrasonic S -wave transducers polarized and aligned in the horizontal direction, with a centre frequency of 1 MHz. Due to the specific orientation of the transducers, the dominant recorded energy represents SH -wave arrivals. This allows us to consider scalar wave propagation and, thus, to use relation (3). We place one receiver at the top of the sandstone (or cement) plate and 17 sources at the bottom of the aluminium plate with a spacing of 2.5 mm. The transducers are attached to the sample using an S -wave couplant from Panametrics. Each source transmits a sine wave signal, with a centre frequency of 1 MHz, from an Agilent 33210A function generator, which is afterwards amplified by

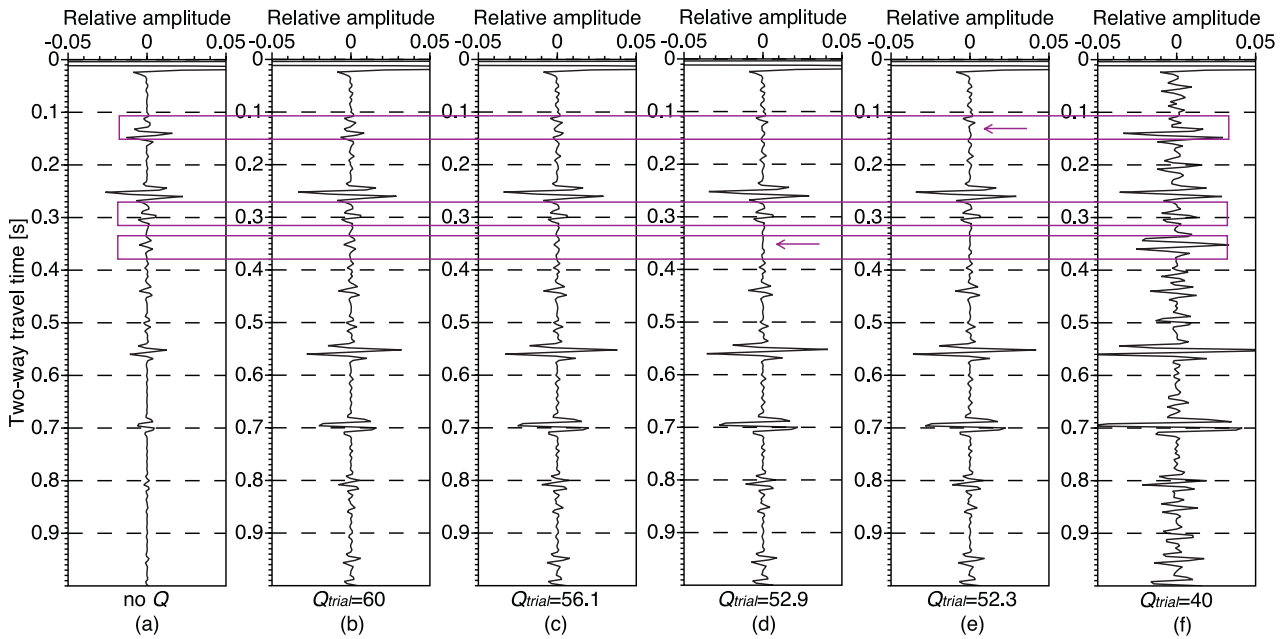


Figure 5. As in Fig. 4, but for the model for the monitor survey. (b)–(f) Retrieved results with Q compensation with Q_{trial} equal to 60, 56.1, 52.9, 52.3 and 40, respectively.

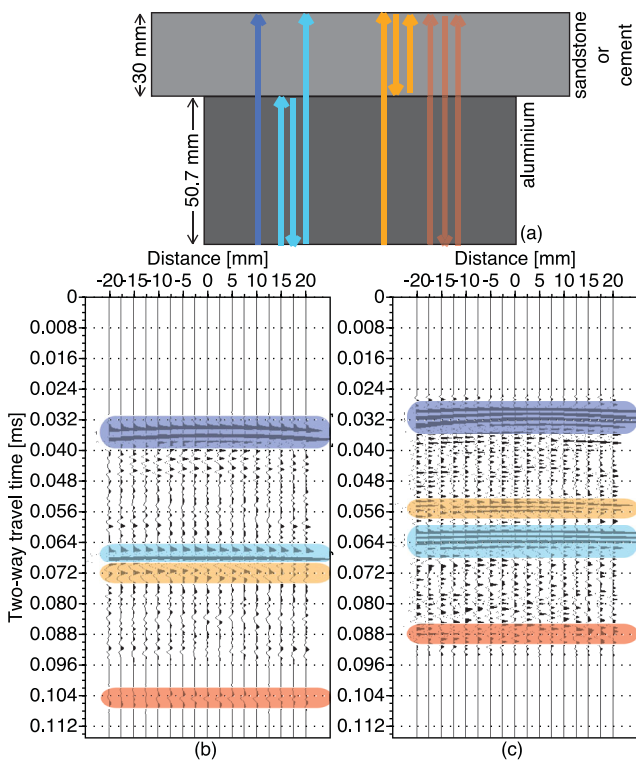


Figure 6. (a) Sketch of the laboratory two-layer sample with a bottom layer of 50-mm aluminium and a top layer of 30-mm sandstone or cement. The coloured arrows depict travel paths of the first few arrivals. Measured transmission responses when using a top layer of (b) Felsler sandstone (base survey) and of (c) Portland cement (monitor survey). The amplitudes are clipped for visualization purposes. The coloured transparent areas highlight arrivals corresponding to the coloured arrivals in (a).

50 dB by an EN 2100L RF amplifier. The transmission responses are recorded on a Yokogawa DL4200 oscilloscope for 0.2004 ms with a sampling rate of 20 ns. After application of source–receiver reciprocity, the measurement geometry we use in this experiment can be seen as a down-scaled model of the situation presented in Section 2.2 with an impulsive source at the Earth’s surface, receivers along a horizontal well in the subsurface, and a changing subsurface layer. From separate transmission measurements directly on sandstone, cement and aluminium plates we calculate S -wave propagation velocities of 1625, 2470 and 3170 m s^{-1} , respectively. From the weight and the volume of the sandstone plate, we calculate its density to be 2370 kg m^{-3} . From the literature, we take density for the cement as 1500 kg m^{-3} and for aluminium—2700 kg m^{-3} .

Figs 6(b) and (c) show the first 0.115 ms of the transmission responses at the receiver from the transducer sources, while in Fig. 6(a) we show the interpretation of the different arrivals. The interpretation is performed by calculating the expected arrival times from the measured propagation velocities in the plates and their known thicknesses. Due to the wave attenuation inside the sandstone and cement layers, the later arrivals are weak compared to the direct arrival. For visualization purposes, the amplitudes of the arrivals are clipped at 20 per cent for the aluminium/sandstone and at 5 per cent for the aluminium/cement sample of the amplitude with respect to the direct arrival. In the result from the aluminium/sandstone sample, the arrival with the apex at 0.036 ms (dark blue) is the direct S -wave arrival and the arrival at 0.068 ms (light blue) is the event recorded after internal reflection inside the aluminium; the arrival at 0.073 ms (orange) is the multiple of the first arrival after reflection at the bottom of the sandstone, while the arrival at 0.105 ms (red) has traversed both layers three times. The interpretation of the respective arrivals in Fig. 6(c) uses the same colour coding.

When applying the Q -estimation procedure to the recorded transmission panels, different sources of error might influence the results:

(i) At source positions further away from the receiver, we see the appearance of converted arrivals, which might arise in practical field applications as well. Such arrivals might interfere with ghost

arrivals we want to use for velocity and Q -estimation and lead to incorrect estimation.

(ii) There is weak direct converted S -to- P energy in the recorded responses caused by imperfect coupling of the transducers to the samples. This event is more easily noticeable at times earlier than the direct S -wave arrivals. Correlation of such converted arrivals with the events of interest might retrieve events interfering with the ghosts which we need for the Q -estimation procedure and thus again lead to incorrect estimation.

(iii) As explained in the previous section, when applying the Q -estimation procedure the summation of the individual ghost components should result in the cancelation of the final retrieved ghost when a transmission panel is amplified with Q_{trial} equal to the Q of the sandstone or the cement. To achieve a complete cancelation, also higher-order multiply reflected arrivals need to be recorded and correlated. Relation (3) is derived for an open system. Strictly speaking, our laboratory models represent closed systems, so we should not use relation (3), but instead a relation similar to eq. (13) from Ruigrok *et al.* (2008), where one of the Green's functions inside the integral is such that the influence of the free surface has been eliminated. When this is not done, the contribution of the higher-order multiply reflected arrivals (later individual ghost components) to the retrieved final ghost is still significant and this ghost will not disappear even in a lossless media. Application of the Q -estimation procedure in this case would result in an erroneous Q .

(iv) Further complication that might arise is that when the measured transmissions are gained with Q_{trial} before correlation, the off-plane later arrivals are also gained and their contribution to the retrieved result might interfere with the ghosts, thus also resulting in an erroneous estimation of Q .

(v) Yet another complication can be detected by looking at Figs 6(b) and (c)—due to the strong attenuation, the red arrival is already very weak and close to the level of the background noise. Gaining with Q_{trial} of the later contributions to the final retrieved ghost, which are already at the noise level, will result effectively in gaining of the noise and thus again in erroneous estimation of Q .

To minimize the influence of the various sources of error listed above, we restrict the correlation process only to the blue, orange and red arrivals. We achieve this by muting all arrivals earlier than the direct S -wave and later than the red arrivals. For the survey with the aluminium/sandstone sample, the second multiple from inside the aluminium arrives before the red arrival at 0.099 ms. For this sample, we mute also this arrival, see Fig. 6(b). Muting the later arrivals eliminates also the later reflections from the side walls, so this process can be seen as 'opening' the samples by removing their side walls. This makes the utilization of relation (3) justified. Note that the first reflections from the side walls, recorded at around 0.076 ms in Fig. 6(b) and at 0.05, 0.066 and 0.083 ms in Fig. 6(c), should also be muted if, in the retrieval process, they are expected to interfere with ghosts we want to retrieve. For our samples this is not the case and we do not mute them.

The muting process limits the used arrivals only to the dark blue/light blue and orange/red ones. The correlation of the dark blue arrival with the light blue arrival retrieves one of the ghost components that are kinematically identical to an internal reflection from the bottom of the aluminium layer as if measured with coinciding source and receiver directly at the top of the aluminium. The correlation of the orange and the red arrivals retrieves the other ghost component, which coincides in time with the first ghost component, but has an opposite polarity. Using only these two ghost components

means that the cancelation of the final ghost would be incomplete for the correct Q_{trial} , as the ghost obtained from the red/orange arrivals is weaker than the ghost obtained from the dark blue/light blue arrivals. Consequently, the Q -estimation procedure will result in a Q -value that is lower than the actual Q -value. Nevertheless, knowing the propagation velocity and density of the two layers allows us to calculate the expected error. This is done by calculating the reflection and transmission coefficients at the boundaries and using them to calculate the amplitudes of the expected dark blue/light blue and orange/red ghost arrivals in a lossless medium. The ratio of these two arrivals provides an initial estimate of the error one would obtain using the Q -estimation procedure. In such a way, we calculate for the aluminium/sandstone sample an error of 21.1 per cent and for the aluminium/cement sample—23.4 per cent. Note that, in the error calculations, we assume that the velocity and Q are frequency-independent.

We apply relation (3) to both measured transmission panels (Figs 6b and c). We autocorrelate the measured responses, sum the correlation results along the source positions (after tapering the autocorrelations to zero for sources at both ends) and take the positive times only. The results are the leftmost traces in Fig. 7 for sandstone (top) and cement (bottom) plates. Correlation of the dark blue arrival with the orange arrival results in the retrieval of the physical reflection from the bottom of the sandstone or cement plates (highlighted with orange in the figures) as if recorded at the receiver from a virtual source coinciding with it. The retrieved ghost is highlighted in blue in the figures. As can be seen in Fig. 7, the ghost reflection is retrieved for both data sets at two-way traveltime of 0.032 ms. Dividing the thickness of the aluminum plate by half of the two-way traveltime gives 3170 m s^{-1} , which is the propagation velocity inside the aluminium. The change in the velocity of the top layer, because of the change of material from sandstone to cement, did not affect the estimate of the layer-specific velocity inside the aluminium. From this we can confidently conclude that the changes in the subsurface velocities have occurred only inside the top layer.

The results from the application of the Q -estimation procedure to the muted transmission panels from Figs 6(b) and (c) are shown in Figs 7 top and bottom rows, respectively. Due to the multiplication of the transmission panels with an exponentially increasing function, for visualization purposes, each result has been normalized to its maximum amplitude at time $t = 0 \text{ s}$ and further clipped at the strongest positive and negative peaks between the physical reflection and the ghost.

First we discuss the results from for the aluminium/sandstone sample. Looking at the behavior of the wavelet of the retrieved physical reflection from the bottom of the sandstone for $Q_{\text{trial}} = 90, 80, 70, 60, 50, 40, 30, 20$ (top row in Fig. 7), we can see that it preserves its polarity and its strongest negative peak at 0.0365 ms. The wavelet's positive peak at 0.0352 s appears to become weaker compared to the peak at 0.0376 s; we attribute this to the interference with the changing wavelet of the ghost from inside the aluminium. Following the behavior of the ghost wavelet for the different Q_{trial} -values, we notice that its strength relative to the physical reflection diminishes for Q_{trial} -values down to 30, but for $Q_{\text{trial}} = 20$ the ghost again starts gaining in amplitude relative to the physical arrival. The ghost does not completely disappear with changing Q_{trial} as is the case in the modelling results. However, its wavelet changes its character—the positive peak at 0.032 s turns from dominant for high Q_{trial} to nearly equal to the wavelet's negative peak at 0.0336 s; the wavelet's negative peak at 0.0336 s also grows relative to the wavelet's negative peak at 0.0312 s. To decide which value of Q_{trial} should be taken as the outcome, we further examine the

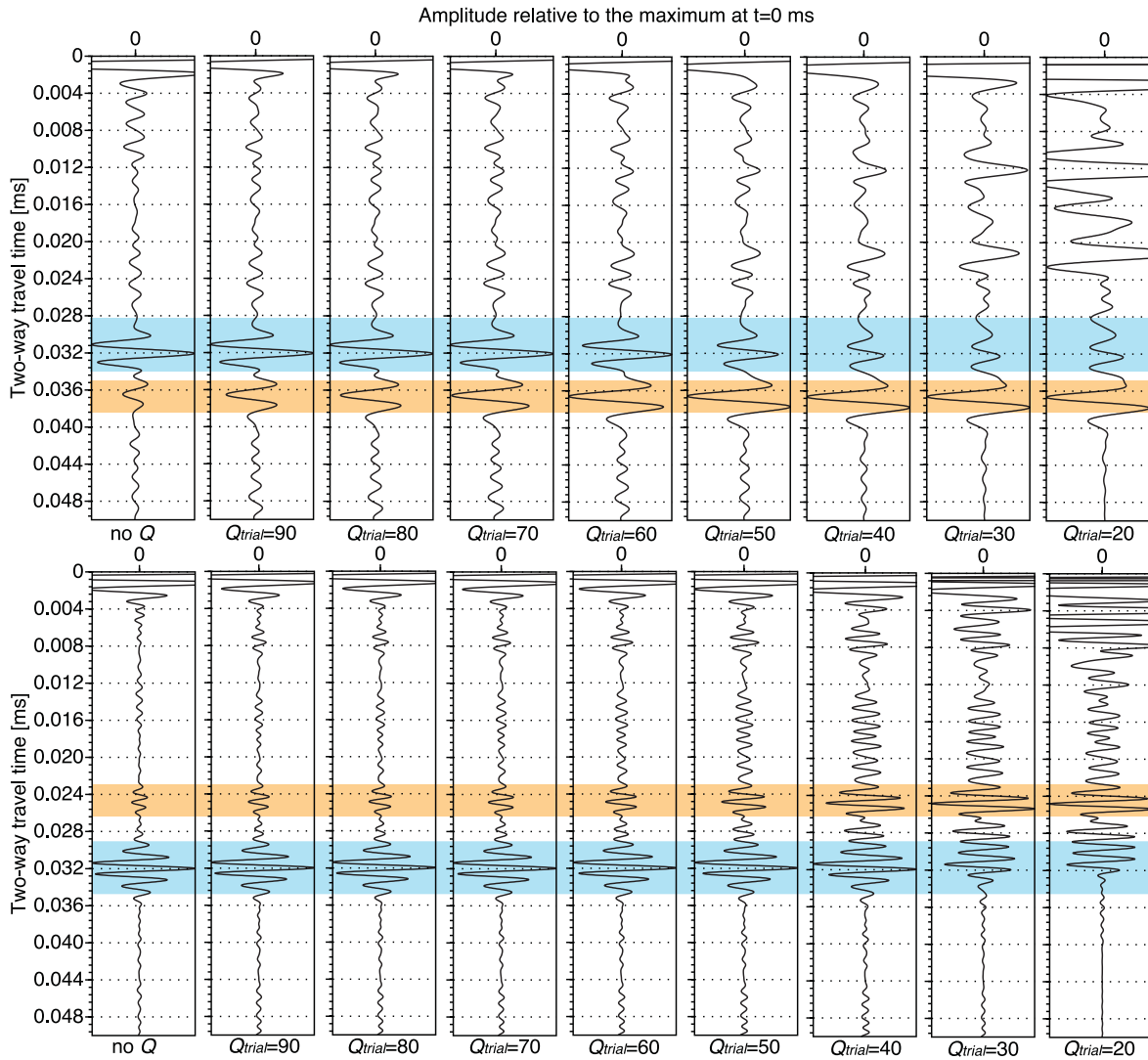


Figure 7. Q -estimation procedure for the recordings on the aluminium/sandstone sample (top panel) and the aluminium/cement sample (bottom). The Q_{trial} values used are indicated below each trace. The physical reflection from the bottom of the sandstone (top row) or the cement (bottom row) is highlighted by light orange, while the ghost from inside the aluminium is indicated in light blue. The traces are shown after normalizing the amplitudes to the maximum, which is at $t = 0$ ms, and clipping at the strongest positive and negative peaks between the physical reflection and the ghost.

behavior of the ghost's wavelet for Q_{trial} -values between 40 and 30, see Fig. 8(a). Following the changes in the wavelet for the different Q_{trial} -values, we see that the negative peaks at 0.0312 and 0.0336 ms become equal in amplitude for $Q_{\text{trial}} = 34$; for lower values, the later peak becomes stronger. Choosing the value 34 as the outcome from the Q -estimation procedure and correcting it for the 21.1 per cent error, we obtain the sandstone's $Q_{\text{SI}} = 41$ (after rounding off). To obtain an independent estimate of the sandstone's Q , we apply the spectral-ratio method to measurements taken only over the sandstone plate. We record the direct transmission and its multiple that has reflected from the top and bottom of the sandstone. We apply geometrical-spreading correction to the two arrivals, select them using a narrow time window, take their amplitude spectra (Fig. 9a) and plot the log of their amplitude ratio (Fig. 9c). Using the slope, we estimate $Q_{\text{SR}} = 47$ (after rounding off). In Fig. 9(a), the peaks of the two spectra are not at 1 MHz but at lower frequencies, as the waves have already experienced the effect of attenuation of the higher frequencies due to the propagation from the source to the receiver.

We now look at the Q -compensation results for the ghost for the aluminium/cement sample, shown in bottom row in Fig. 7. We notice that the change in the behavior of the ghost wavelet is easier to observe here when compared to the top row. We also see that the ghost diminishes in amplitude relative to the physical reflection for lower Q_{trial} -values, but for the lowest values of 30 and 20 it again starts growing relative to the physical arrival. Furthermore, at the beginning of the Q -compensation procedure, the ghost's strongest peak is positive and at 0.032 ms, while for the lowest Q_{trial} -values the strongest peak is negative and at 0.0314 ms. To decide which Q_{trial} -value we can pick from the procedure, we concentrate on the positive peaks at 0.0308 and 0.032 ms, see Fig. 8(b). We see that the peak at 0.0308 s becomes equal in amplitude to the one at 0.032 s at $Q_{\text{trial}} = 31$ and for lower values of Q_{trial} is stronger. Choosing value 31 as the outcome from the Q -estimation procedure and correcting it with 23.4 per cent, we obtain, after rounding off, the cement's $Q_{\text{SI}} = 38$. Applying the SR method to the transmission measurements made directly over the cement plate (see the spectra in Figs 9b and d), we estimate $Q_{\text{SR}} = 35$.

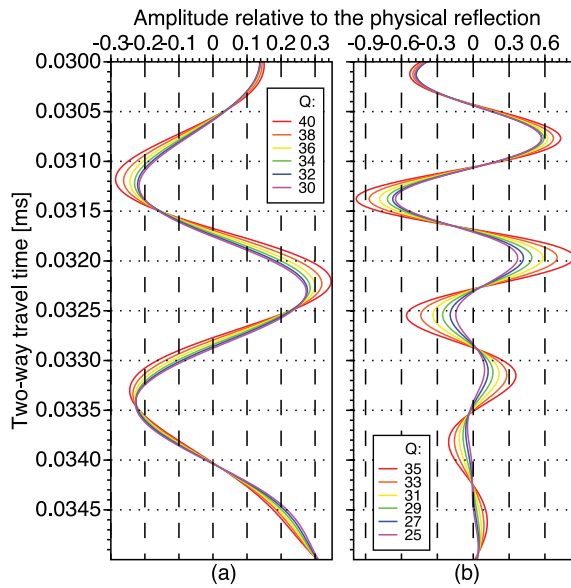


Figure 8. Changes in the ghost wavelet during the Q -estimation procedure for a compensation with Q_{trial} -values as indicated by the color coding for a sample with a top layer of (a) sandstone and (b) cement.

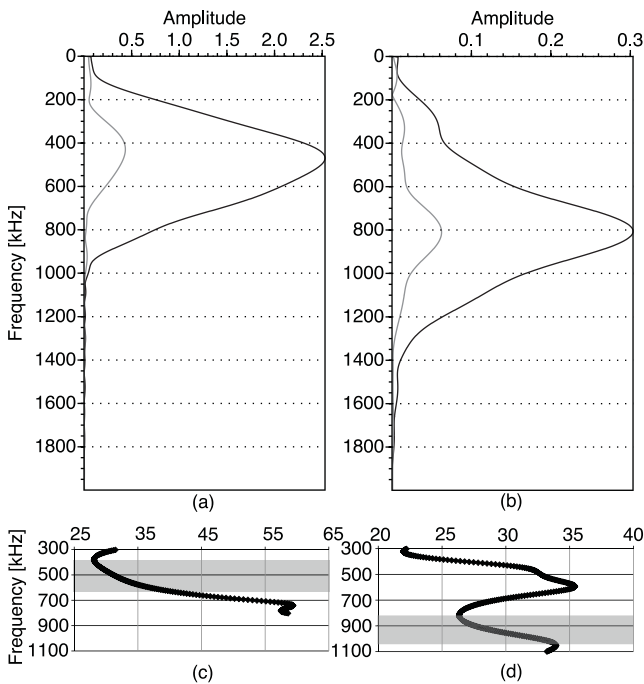


Figure 9. Amplitude spectra, after application of geometrical-spreading correction, for the direct transmission (black) and its multiple (gray) over 30 mm of (a) Felsler sandstone and (b) Portland cement. (c) Log ratio of the spectra in (a). (d) Log ratio of the spectra in (b). The transparent grey areas indicate the frequency interval used for estimation of the quality factor by the spectral-ratio method.

From the comparison of the Q -values estimated from the SI and the SR method, we see that the SI Q -compensation procedure can extract the quality factor of multi-layered physical models. The measurements we use here are an extreme case, as the damping of the waves is very high for such high frequencies. Due to this very strong damping, the layer's internal reflection arrivals are weak and close to the level of the noise. This would cause uncertainties in the estimates of Q_{SI} . But such uncertainties will also affect Q_{SR} ,

as this estimate also depends on the multiple reflection inside the sandstone and cement plates.

4 DISCUSSION

In the previous sections, we present a method to monitor changes in velocity and Q using ghosts in the SI results. We make use of eq. (3), as it is derived for full wavefields and thus accounts for scattering losses. We use the fact that the ghosts can be distinguished from the physical reflections when intrinsic losses are present in the medium. This distinction, but also the accounting for the scattering losses, is very dependent on the available receiver aperture for integration in eq. (3). The ghosts due to the intrinsic losses are caused by reflections inside subsurface layers. With insufficient receiver aperture, the ghosts will be retrieved even in lossless media and thus would not allow us to use them for monitoring. To avoid this problem, we choose the geometry we present here with one source at the surface and multiple receivers in the subsurface.

The method we propose will work best with SI for full wavefields. SI with wavefield separation would produce the ghosts that we are after only when there is no scattering between the source at the surface and the receivers at depth. Such is the case for ocean-bottom acquisition. When there is scattering between the source and the receivers, application of wavefield separation like in Bakulin & Calvert (2006) or in Mehta *et al.* (2007), that is, using scattering-theory SI (Vasconcelos *et al.* 2009), would retrieve the ghosts we are interested in even in a lossless medium. As shown by Vasconcelos *et al.* (2009), for the general case of having the receivers inside the scattering domain (in wells) to avoid the appearance of the ghosts in the lossless case, sources in the complete domain are required. As this will not likely be the case, in practice the ghosts will always be present and thus SI with wavefield separation would not be applicable for monitoring change in Q using our approach. Nevertheless, it can still be used for monitoring changes in velocity. For the purpose, though, the ghosts should be identified and connected to subsurface layers. This can be achieved with the technique we propose with a vertical well.

To recognize the ghosts as such and to connect them to specific layers, we propose to make use of a source at the surface and receivers in a vertical well. From the reversal of polarity of the ghost from receiver position above and below a specific layer, we recognize the layer which is responsible for the appearance of the ghosts due to the intrinsic losses. When the receivers are above the layer, the ghost arises due to violation of the assumption in relation (3) of a homogeneous medium below the receiver. Because of this, that part of the ghost will be present for both lossless and lossy medium. For receivers below the layer, the ghost will be present only if there are intrinsic losses between the receiver and the layer. This also means, that in a lossy media, if a ghost event reverses its polarity then there is a change of the seismic parameters at this point, for example at the beginning of a new layer.

In the ultrasonic laboratory example, the ghost does not disappear during the Q -compensation procedure the way it does in the numerical example. The sandstone and the cement are porous materials and, strictly speaking, they should be considered as poroelastic. Due to this, the intrinsic losses might cause the wavelet for different arrivals to vary. This phenomenon will be stronger in the red and orange arrivals in Fig. 6(a) compared to the blue arrivals, as the former traverses the lossy material three times compared to one time by the latter. The changes in the wavelet might be a cause why the ghost does not disappear and as a consequence lead to interpreter-

related errors in the Q -estimation due to the difficulty in picking the right Q_{trial} value in Fig. 8. If we take the value of $Q_{\text{SR}} = 47$ as a reference value for the quality factor in the sandstone, $Q_{\text{trial}} = 36, 35, 34, 33$ after correction will give Q -values of 44, 42, 41 and 40 or errors of 6, 11, 13 and 15 per cent, respectively. For the cement, using a reference value of $Q_{\text{SR}} = 35$, Q -values of 41, 39, 38 and 37 (after correction) will result in estimation errors of 17, 11, 9 and 6 per cent, respectively. The SR method is also prone to interpreter errors. Figs 9(c) and (d) show the complete log amplitude ratio of the spectra between the first arrival and its multiple. The slope of these ratios would be very different depending on which part of the spectrum is used for calculation of Q . The Q -value of 47 for the sandstone is calculated from the slope of the spectral ratio between 400 and 600 kHz. If the frequency range were taken between 350 and 600 kHz or between 400 and 650 kHz, the Q -values calculated from these slopes would be 56 and 37, respectively. This would translate to errors of 19 and 21 per cent, respectively. For the cement, we calculate Q of 38 using the slope between 800 and 1050 kHz. If the spectral range were chosen between 750 and 1050 kHz or between 800 and 1100 kHz, then the estimated Q -values would have been 45 and 39, respectively. These values would give respective errors of 18 and 2 per cent. This shows that the SR method might be more sensitive to interpreter-choice errors than the SI Q -estimation method.

5 CONCLUSIONS

We showed how the layer-specific changes in velocity and quality factor Q can be monitored using non-physical arrivals (ghosts) in the results retrieved using SI. We illustrated this using numerical-modelling data from an active source at the surface and multiple geophones inside a vertical and a horizontal well. We used the SI procedure to create a virtual zero-offset trace at the position of the surface source. We showed that the retrieved response from the receivers inside the vertical well could be used to pinpoint which non-physical arrival was caused by which subsurface layer. Using the retrieved responses from the receivers in the horizontal well, we showed how to estimate the changes in velocity and Q for each layer. The latter was achieved by compensating the measured transmission panels with trial Q values before application of SI, while we estimated the former directly from the retrieved ghosts. These ghosts represent reflections from inside each of the subsurface layers, as if measured with source and receiver positioned directly on top of each of the layers. We applied the layer-specific estimation procedure to ultrasonic laboratory data measured on aluminium/sandstone and aluminium/cement samples and obtained estimates of layer-specific velocity and Q . These estimates are close to the ones obtained using the spectral-ratio method.

ACKNOWLEDGMENTS

The work of ER is supported by The Netherlands Organization for Scientific Research NWO (grant Topalent 2006 AB). We thank Dylan Mikesell and Ivan Vasconcelos for the very useful comments that helped improve the manuscript.

REFERENCES

- Aki, K. & Richards, J.P., 2002. *Quantitative Seismology*, 2nd edn, University Science Books, Sausalito, CA.
- Bakulin, A. & Calvert, R., 2004. Virtual source: new method for imaging and 4D below complex overburden, in *Proceedings of the 74th Annual International Meeting Expanded Abstracts*, pp. 2477–2480, SEG.
- Bakulin, A. & Calvert, R., 2006. The virtual source method: theory and case study, *Geophysics*, **71**, SI139–SI150.
- Bharadwaj, P., Schuster, G., Mallinson, I. & Dai, W., 2011. Theory of supervirtual refraction interferometry, *Geophys. J. Int.*, **188**, 263–273.
- Campillo, M. & Paul, A., 2003. Long-range correlations in the diffuse seismic coda, *Science*, **299**, 547–549.
- Claerbout, J.F., 1968. Synthesis of a layered medium from its acoustic transmission response, *Geophysics*, **33**, 264–269.
- Curtis, A. & Halliday, D., 2010. Source-receiver wave field interferometry, *Phys. Rev. E*, **81**, 046601, doi:10.1103/PhysRevE.81.046601.
- Dong, S., Sheng, J. & Schuster, G., 2006. Theory and practice of refraction interferometry, in *Proceedings of the 76th Annual International Meeting Expanded Abstracts*, pp. 3021–3025, SEG.
- Draganov, D., 2007. Seismic and electromagnetic interferometry—retrieval of the Earth's reflection response using crosscorrelation, *PhD thesis*, Delft University of Technology.
- Draganov, D., Wapenaar, K. & Thorbecke, J., 2004. Passive seismic imaging in the presence of white noise sources, *Leading Edge*, **23**, 889–892.
- Draganov, D., Ghose, R., Ruigrok, E., Thorbecke, J. & Wapenaar, K., 2010. Seismic interferometry, intrinsic losses and Q -estimation, *Geophys. Prospect.*, **58**, 361–373.
- Froment, B., Campillo, M., Roux, P., Gouédard, P., Verdel, A. & Weaver, R., 2010. Estimation of the effect of nonisotropically distributed energy on the apparent arrival time in correlations, *Geophysics*, **75**, SA85–SA93.
- Halliday, D. & Curtis, A., 2009. Seismic interferometry of scattered surface waves in attenuative media, *Geophys. J. Int.*, **178**, 419–446.
- King, S. & Curtis, A., 2012. Suppressing nonphysical reflections in Green's function estimates using source-receiver interferometry, *Geophysics*, **77**, Q15–Q25.
- King, S., Curtis, A. & Poole, T.L., 2011. Interferometric velocity analysis using physical and nonphysical energy, *Geophysics*, **76**, SA35–SA49.
- Mateeva, A., 2003. Thin horizontal layering as a stratigraphic filter in absorption estimation and seismic deconvolution *PhD thesis*, Colorado School of Mines.
- Mehta, K., Bakulin, A., Sheiman, J., Calvert, R. & Snieder, R., 2007. Improving the virtual source method by wavefield separation, *Geophysics*, **72**, V79–V86.
- Mehta, K., Snieder, R., Calvert, R. & Sheiman, J., 2008. Acquisition geometry requirements for generating virtual-source data, *Leading Edge*, **23**, 620–629.
- Mikesell, T.D., van Wijk, K., Calvert, A. & Haney, M., 2009. The virtual refraction: useful spurious energy in seismic interferometry, *Geophysics*, **74**, A13–A17.
- Nichols, J., Mikesell, D. & van Wijk, K., 2011. Application of the virtual refraction to near-surface characterization at the Boise Hydrogeophysical Research Site, *Geophys. Prospect.*, **58**, 1011–1022.
- Ruigrok, E., Draganov, D. & Wapenaar, K., 2008. Global-scale seismic interferometry: theory and numerical examples, *Geophys. Prospect.*, **56**, 395–417.
- Ruigrok, E., Wapenaar, K., van der Neut, J. & Draganov, D., 2009. A review of crosscorrelation and multidimensional deconvolution seismic interferometry for passive data, in *Proceedings of the EAGE Workshop on Passive Seismics*, Limassol, Cyprus.
- Schuster, G.T., 2001. Theory of daylight/interferometric imaging: tutorial, in *Proceedings of the 63rd Conference and Exhibition Extended Abstracts*, pp. A–32, EAGE.
- Schuster, G.T., Yu, J. & Rickett, J., 2004. Interferometric/daylight seismic imaging, *Geophys. J. Int.*, **157**, 838–852.
- Slob, E., Draganov, D. & Wapenaar, K., 2007. Interferometric electromagnetic Green's functions representations using propagation invariants, *Geophys. J. Int.*, **169**, 60–80.
- Snieder, R., 2004. Extracting the Green's function from the correlation of coda waves: a derivation based on stationary phase, *Phys. Rev. E*, **69**, 046610, doi:10.1103/PhysRevE.69.046610.
- Snieder, R., 2006. Retrieving the Greens function of the diffusion equation from the response to a random forcing, *Phys. Rev. E*, **74**, 046620.

- Snieder, R., 2007. Extracting the Greens function of attenuating heterogeneous acoustic media from uncorrelated waves, *J. acoust. Soc. Am.*, **121**, 2637–2643.
- Snieder, R., Wapenaar, K. & Larner, K., 2006. Spurious multiples in seismic interferometry of primaries, *Geophysics*, **71**, S1111–S1124.
- Tatanova, M., Bakulin, A., Mehta, K., Korneev, V. & Kashtan, B., 2008. Reconstructing head waves with virtual source method, in *Proceedings of the 78th Annual International Meeting Expanded Abstracts*, pp. 183–187, SEG.
- Tatanova, M., Mehta, K. & Kashtan, B., 2011. Virtual refraction tomography: application to realistic 3D model, in *Proceedings of the 81st Annual International Meeting Expanded Abstracts*, pp. 4239–4243, SEG.
- Thorbecke, J. & Draganov, D., 2011. Finite-difference modeling for seismic interferometry, *Geophysics*, **76**, H1–H18.
- Tonn, R., 1991. The determination of the seismic quality factor Q from VSP data: a comparison of different computational methods, *Geophys. Prospect.*, **39**, 1–27.
- Vasconcelos, I. & Snieder, R., 2008a. Interferometry by deconvolution. Part 1—theory for acoustic waves and numerical examples, *Geophysics*, **73**, S115–S128.
- Vasconcelos, I. & Snieder, R., 2008b. Interferometry by deconvolution. Part 2—theory for elastic waves and application to drill-bit seismic imaging, *Geophysics*, **73**, S129–S141.
- Vasconcelos, I., Snieder, R. & Douma, H., 2009. Representation theorems and Green's function retrieval for scattering in acoustic media, *Phys. Rev. E*, **80**, 036605, doi:10.1103/PhysRevE.80.036605.
- Wapenaar, K., 2004. Retrieving the elastodynamic Green's function of an arbitrary inhomogeneous medium by cross-correlation, *Phys. Rev. Lett.*, **93**, 254301, doi:10.1103/PhysRevLett.93.254301.
- Wapenaar, K., 2006. Green's function retrieval by cross-correlation in case of one-sided illumination, *Geophys. Res. Lett.*, **33**, L19304, doi:10.1029/2006GL027747.
- Wapenaar, K. & Fokkema, J., 2006. Green's functions representations for seismic interferometry, *Geophysics*, **71**, S133–S146.
- Wapenaar, K., Thorbecke, J., Draganov, D. & Fokkema, J., 2002. Theory of acoustic daylight imaging revisited, in *Proceedings of the 72nd Annual International Meeting Expanded Abstracts*, p. ST 1.5, SEG.
- Wapenaar, K., Slob, E. & Snieder, R., 2006. Unified Green's function retrieval by cross-correlation, *Phys. Rev. Lett.*, **97**, 234301-1–234301-4.
- Wapenaar, K., Slob, E. & Snieder, R., 2008. Seismic and electromagnetic controlled-source interferometry in dissipative media, *Geophys. Prospect.*, **56**, 419–434.
- Zhubayev, A. & Ghose, R., 2010. In-situ soil properties from integrated poroelastic models, in *Proceedings of the 80th Annual International Meeting Expanded Abstracts*, p. 1882, SEG.
- Zhubayev, A. & Ghose, R., 2011. Physics-based integration of shear wave dispersion properties for soil property estimation: laboratory investigation, in *Proceedings of the 81st Annual International Meeting Expanded Abstracts*, p. 1343, SEG.
- Zhubayev, A. & Ghose, R., 2012a. Contrasting behavior between dispersive seismic velocity and attenuation: advantages in subsoil characterization, *J. acoust. Soc. Am.*, **131**, EL170–EL176.
- Zhubayev, A. & Ghose, R., 2012b. Physics of shear-wave intrinsic dispersion and estimation of in-situ soil properties: a synthetic VSP appraisal, *Near Surf. Geophys.*, **10**, doi:10.3997/1873-0604.2012016.